Paper CIT06-0586

MULTI-SCALE MODELING OF THE HEAT AND MASS TRANSFER IN A MONOLITHIC METHANE STEAM-REFORMER FOR HYDROGEN PRODUCTION

Luis Evelio Garcia Acevedo
Departamento de Engenharia Mecânica
Universidade Federal de Santa Catarina
Florianópolis/SC
evelio@labcet.ufsc.br

Amir Antonio Martins Oliveira
Departamento de Engenharia Mecânica
Universidade Federal de Santa Catarina
Florianópolis/SC
amirol@emc.ufsc.br

Abstract. Here we present a heat and mass transfer analysis for the catalytic methane steam-reforming in a porous monolithic reactor. Thermodynamic analysis provides the bounds for temperature, pressure and steam-methane molar ration for optimum operation. However, the reactor operation is also constrained by chemical kinetics and heat and mass transfer limitations. Porous washcoated monoliths have been used for a long time in the automotive industry as catalytic converters for destruction of gas and particulate pollutants. Here we analyze the modeling issues related to a multi-scale porous structure and develop a model able to assess the advantages and drawbacks of using a monolith as support for a catalyst layer for steam-reforming.

Keywords: multi-scale modeling, porous media, steam-reforming, hydrogen, monolithic reactor.
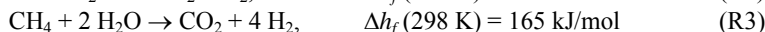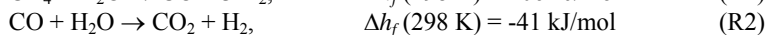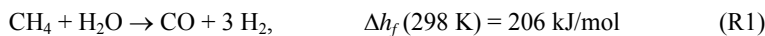
1. INTRODUCTION

Fuel cells have become available as a near future alternative for decentralized energy production. The fuel choice for proton exchange fuel cells (PEM) is hydrogen which has to be provided with sufficient purity. Hydrogen presents several advantages from the environmental point of view, compared to fossil fuels, when used as an energy source for mechanical and electrical decentralized or mobile power production. When used in fuel cells it provides an electrochemical clean, efficient and quiet energy conversion system with zero or ultra-low emissions. As pointed by Biyikoglu (2005), more research is necessary to achieve the desired performance and integration of fuel cell stacks and associated sub-systems, including fuel storage, reforming and processing, air delivery system, heat exchangers, thermal integration, humidification and water management, and DC power processing sensors and controls. A hydrogen production unit by hydrocarbon reforming may be integrated to a small to medium fuel cell systems (under 10 kW) if it is thermally efficient, compact and selective towards hydrogen. Usually, a CO removal operation is always necessary.

Mathiak et al. (2004) (followed by Dokupil et al., 2006) developed an integrated compact reformer-PEMFC system for production of 2.5 kW of electrical power. The steam-reforming reactor was operated at $800^{o}C$ and subsequent water-gas shift (WGS) reactors, a high temperature reactor operating at $400^{o}C$ and a low temperature reactor operating at $200^{o}C$, were used for CO removal. The authors relied heavily on information extracted from industrial scale steam-reformers in which the reacting mixture flows along 7.5 to 12 m long tubes with inner diameter between 7 to 13 cm (Twigg, 1989; Larmine e Dicks, 2000, Kordesh and Simader, 1996). However, in compact steam reformers, a host of different technologies can be used to increase thermal and chemical integration within the reformer, specially an enhanced heat and mass transfer. From these, the use of washcoated monoliths is a promising technology, since they provide high surface area available for catalysis combined to low pressure drop.

Here, we present an analysis of the hydrogen production from the steam-reforming of natural gas in a washcoated monolithic reactor. The monolith provides a continuous solid structure, favoring temperature equalization by conduction heat transfer. The washcoat layer provides a high specific internal surface area increasing the catalytic activity. The analysis is focused to operation conditions able to provide 5 kW of electrical power in a PEM fuel cell. The adequate range for temperature, pressure and steam-methane ratio and the equilibrium concentration of products were determined previously (Garcia and Oliveira, 2006). A heat and mass transfer model, with chemical reaction and heat transfer from the exterior, is then developed to calculate the rates of conversion to products and the thermal and mass transfer limitations of the basic design. The model uses the volume-averaged equations for conservation of thermal energy and mass of chemical species and properly accounts for the multi-scale nature of the porous monolith through a combined microscopic-macroscopic treatment for the diffusion-reaction. A treatment for internal diffusion in catalyst particles has been used previously in the modeling of adsorption enhanced steam reforming. Xiu et al. (2002) uses a simplified diffusion model, which is extended in Xiu et al. (2003). The authors point out the excessive

computational CPU time to solve the detailed treatment. Here, an equivalent to an intra-particle model is developed for a monolith reactor, which is then simplified taking into account the multi-scale nature of the monolith.

A reduced mechanism for the steam reforming including five chemical species (CH_4, H_2O, H_2, CO, CO_2) and three global reaction rates is assumed. These are the steam reforming (R1), the water gas shift reaction (R2) and the methanation reaction (R3):

$$CH_4 + H_2O \rightarrow CO + 3\ H_2, \qquad \Delta h_f\ (298\ K) = 206\ kJ/mol \qquad (R1)$$
$$CO + H_2O \rightarrow CO_2 + H_2, \qquad \Delta h_f\ (298\ K) = -41\ kJ/mol \qquad (R2)$$
$$CH_4 + 2\ H_2O \rightarrow CO_2 + 4\ H_2, \qquad \Delta h_f\ (298\ K) = 165\ kJ/mol \qquad (R3)$$

The methanation reaction is the global steam-reforming reaction to saturated products. Chemical kinetics and adsorption constants are obtained from the literature for nickel-alumina based catalysts. A comparison of the different sets of parameters available in the literature (Garcia, 2006) showed the expected variation in behavior exhibited by different catalytic particles and reactor conditions. Here, a given set of parameters, also used by other authors, were used as a basis to analyze the reactor performance and to compare different geometric and operation conditions.

A thermodynamic analysis presented elsewhere (Garcia and Oliveira, 2006) verified the equilibrium conditions associated to the production of hydrogen to power a 5 kW PEM fuel cell operating at 80°C with 50% efficiency. The reforming unit analyzed consisted of water and methane heaters, a water evaporator for steam production, a steam and methane super-heater, a methane steam reformer and an external combustion reactor to produce the amount of heat needed for the heating, phase change and reforming operations. That analysis assumed that the reformer remains isothermal at the reforming temperature set. Table 1 summarizes the operation conditions assumed for the reforming reactor and the equilibrium performance parameters that are obtained.

Table 1: Operation parameters and equilibrium performance parameters for the steam-reforming reactor (Garcia and Oliveira, 2006).

Reforming reactor operation parameters:			
Reforming pressure	P,	atm	1.2
Reforming temperature	T,	°C	700
Inlet steam-to-methane molar ratio	R		4
Equilibrium conditions at reactor outlet:			
Outlet hydrogen number of moles	n_{H2},	moles	3.469
Dry-basis outlet hydrogen mole fraction	X_{H2}		0.7764
Equilibrium results for a PEMFC producing 5 kW at $T_{cel} = 80$°C, $\eta_{cel} = 0.5$:			
Reformer outlet hydrogen mass flow rate	m_{H2},	kg/s	8.7×10^{-05}
Total inlet mass flow rate of methane	m_{CH4_T},	kg/s	3.3×10^{-04}
Inlet mass flow rate of water	m_{H2O},	kg/s	9.2×10^{-04}
Reformer efficiency:			
Reforming reactor efficiency	η_{ref}		0.6

In Table 1, m_{H2} is the required equilibrium reformer outlet hydrogen mass flow rate to power a 5 kW PEMFC operating at 80°C with 50% cell efficiency. The total mass flow rate of methane m_{CH4_T} includes the mass flow rate of methane needed for the reforming reactions as well as the auxiliary mass flow rate of methane needed for water and methane heating from 298 K, for water phase change and also to provide the necessary thermal energy to keep the reforming reaction isothermal.

The values listed in Table 1 are used here as reference values. This analysis provides the framework for the reactor sizing and for establishing the adequate operation conditions. The solid carbon production is not taken into account in the chemical kinetic mechanism. Therefore, deactivation by coke formation is not explored.

3. HEAT AND MASS TRANSFER ANALYSIS

The thermodynamic analysis provides the equilibrium values of concentration and heat transfer rates. However, it does not provide the rates at which chemical reaction, mass transfer and heat transfer occurs. The proper rector design requires a transport model. Figure 1 presents a rendering of the monolith reactor under analysis. The monolith is formed by a large number of square cross section channels which span the entire reactor length. A washcoat layer, formed by alumina particles impregnated with nickel crystals, coats each channel's walls. The flow of the reacting mixture occurs along the channels (x direction). Mass transfer by diffusion allows the reacting species to reach the catalytic sites within the washcoat (along the z direction). There, the conversion to products occurs and they diffuse back to the channel where they are advected out. In the model developed all reaction occurs catalytically within the washcoat.
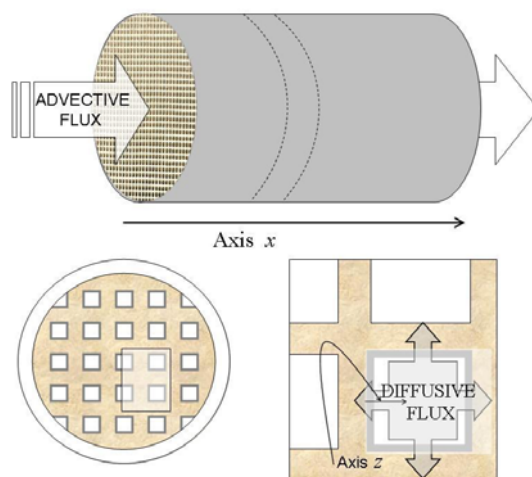
Figure 1: Rendering of the monolith reactor under analysis showing the channels and the *x* and *z* axis.

The model developed combines a macroscopic and a microscopic treatment. The macroscopic treatment considers the effects of heat and mass transfer in the channels and the monolith. Figure 2 presents a rendering of an enlarged view of the monolith, showing the channel, the washcoat (active) layer and the inert walls. The macroscopic treatment considers the gas inside the channels as the β phase, and the solid monolith as the σ+τ phase. In the β phase heat transfer by conduction and advection occurs. Mass transfer occurs by diffusion and advection. In the σ+τ phase there is heat transfer by conduction and thermal energy generation by chemical reaction. The kinetics of the chemical reactions is accounted for in the microscopic treatment.
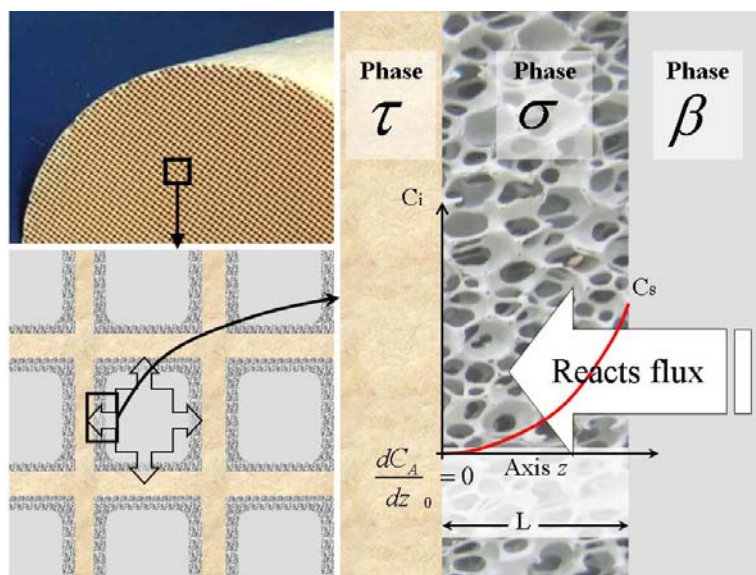

Figure 2. Enlarged view of the monolith, showing phases β (gas within the channels), σ (washcoat (active) layer) and τ (the inert monolith wall).

The microscopic treatment is diffusion-reaction problem in the washcoat. Figure 3 presents a rendering of the channel (with dimensions *h* and *b*), the washcoat (with thickness L_σ) and the inert walls. The insert shows that the washcoat layer (σ phase) is formed by a gas phase, phase γ, and by a solid catalytic layer, phase ω. Note that, volumetrically, γ+ω = σ. For the microscopic model, there is mass transfer by diffusion across an effective medium (phase σ) and surface chemical reaction at the γω interface. The temperature of the washcoat layer is assumed uniform and equal to the σ+τ phases (solid monolith phase) temperature calculated from the macroscopic model in a local *z* coordinate. The surface mass flux at the β-σ interface is passed to the macroscopic model as a source term in the species mass conservation equation. The thermal energy produced (or absorbed) at the γω interface in applied to the macroscopic model solid energy equation (σ+τ phase) also as a source term. This model considers that there is separation of length scales. In Figure 3, *b* and *h* are the channel cross section width and height, L_σ is the washcoat layer

thickness, L_β is the channel length (equal to the monolith length) and D is the monolith diameter. The separation of length scales requires that

$$L_\sigma << (b\,,\,h) << (L_\beta\,,\,D)$$

This separation of length scales allows for writing two sets of equations whose solutions are coupled through the β-σ interface.
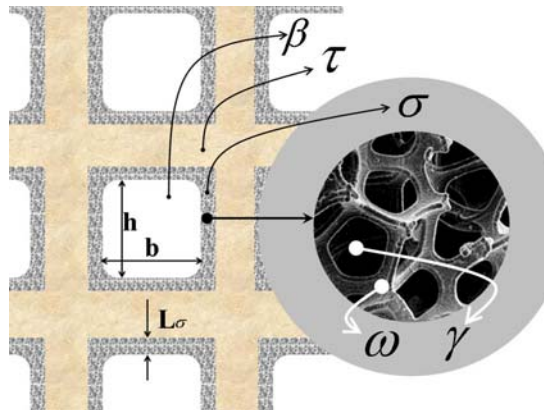

Figure 3. Rendering of the channels cross section. The magnification of the washcoat layer shows phases γ (gas within the washcoat) and ω (solid particles).

3.1 MACROSCOPIC MODEL

The macroscopic model is based on volume-averaged transport equations. The variables listed below are volume-averaged over a suitable representative elementary volume (Kaviany, 1995). Since the permeability of the monolith is high, pressure drop along the channels is negligibly small and therefore a volume-averaged momentum equation is not solved.

Gas phase mass conservation:

For a one-dimensional flow in a uniform porosity porous medium, the volume-averaged mass conservation equation becomes:

$$\frac{\partial\left(\varepsilon_\beta\rho_g\right)}{\partial t}+\frac{\partial}{\partial x}\left(\varepsilon_\beta\rho_g u_g\right)=0 \qquad\qquad 1$$

where ε_β is the porosity of the monolith (volume of monolith channels divided by the total volume of the monolith) and ρ_g and u_g are the gas mixture density and velocity respectively. The gas phase velocity in the monolith channels is equivalent to the intrinsic phase-averaged velocity in the β phase (Kaviany, 1995).

Gas phase species i mass conservation:

The volume-averaged one-dimensional advection-diffusion equation with chemical reaction for the conservation of mass of a chemical species *i* is:

$$\frac{\partial}{\partial t}\left(\varepsilon_\beta\rho_g Y_i\right)+\frac{\partial}{\partial x}\left(\varepsilon_\beta\rho_g u_g Y_i\right)=\frac{\partial}{\partial x}\left(\varepsilon_\beta\rho_g\left(D_{im}+D_{x,m}\right)\frac{\partial Y_i}{\partial x}\right)+\varepsilon_\beta\dot{w}_{r,i,\beta} \qquad\qquad 2$$

where Y_i is the species *i* intrinsic volume-averaged mass fraction, D_{im} is the species *i* molecular mass diffusion coefficient in the mixture, $D_{x,m}$ is the gas mass axial dispersion coefficient and $\dot{w}_{r,i,\beta}$ is the species *i* volume averaged reaction rate.

Gas phase thermal energy conservation:

The one-dimensional volume-averaged energy equation for the gas phase assumes thermal non-equilibrium between the gas and solid phases. This thermal non-equilibrium is modeled by an interfacial surface-convection heat transfer coefficient. The equation includes a transient term, the advection of thermal energy along the channels, the heat transfer by conduction along the channels, including the effect of thermal axial energy dispersion, and interfacial surface-convection heat transfer with the solid phase. It is written as:

$$\frac{\partial}{\partial t}\left(\varepsilon_\beta \rho_g c_{pg} T_g\right) + \frac{\partial}{\partial x}\left(\varepsilon_\beta \rho_g u_g c_{pg} T_g\right) =$$
$$\frac{\partial}{\partial x}\left(\varepsilon_\beta \left(\lambda_g + \rho_g c_{pg} D_{x,T}\right)\frac{\partial T_g}{\partial x}\right) + \left[h_{sg}\left(\frac{S_{\beta\sigma}}{\varepsilon_\beta}\right)\left(T_s - T_g\right)\right]\varepsilon_\beta \qquad 3$$

where λ_g is the molecular gas thermal conductivity of the mixture, $D_{x,T}$ is the energy axial dispersion coefficient, h_{sg} is the interfacial heat transfer coefficient between gas and solid phase, and $S_{\beta\sigma}$ is the specific interfacial area between the gas and solid phases.

Solid phase thermal energy conservation:

The one-dimensional volume-averaged energy equation for the solid phase includes a transient term, the axial heat transfer by conduction along the solid part of the monolith, interfacial surface-convection heat transfer with the gas phase in the channels, thermal energy generation (absorption) due to the reforming reactions in the washcoat and an external heat transfer to the environment. It is written as:

$$\frac{\partial}{\partial t}\left(\left(1-\varepsilon_\beta\right)\rho_s c_{ps} T_s\right) =$$
$$\frac{\partial}{\partial x}\left(\left(1-\varepsilon_\beta\right)\lambda_s \frac{\partial T_s}{\partial x}\right) - \left[h_{sg}\left(\frac{S_{\beta\sigma}}{\varepsilon_\beta}\right)\left(T_s - T_g\right)\right]\varepsilon_\beta + \left(\Delta h_{r,i} \dot{w}_{r,i,\beta}\right)\varepsilon_\beta - \left[\frac{h_e P_m}{A_m}\left(T_s - T_\infty\right)\right] \qquad 4$$

where ρ_s is the solid density, λ_s is the molecular thermal conductivity; $\Delta h_{r,i}$ is the heat of reaction associated to species i, h_e is the monolith external heat transfer coefficient, T_∞ is the monolith external ambient temperature, P_m is the monolith external perimeter and A_m is the monolith external surface area. The external heat transfer coefficient accounts for, in an approximate way, the overall heat transfer to the external heat source (methane-air combustion).

The boundary conditions for the macroscopic model include prescribed temperature and concentrations at the inlet and parabolic conditions at the outlet. Zero heat transfer is assumed from the solid at the outlet. They are written as:

At x = 0,
(1) $m_g = \rho_g A_m u_g = m_{g,o}$
(2) $Y_i = Y_{i,o}$
(3) $T_g = T_{g,o}$ 5
(4) $\partial T_s / \partial x = 0$
At x = L_m,
(5) $\partial Y_i / \partial x = \partial T_g / \partial x = \partial T_s / \partial x = 0$

Initial conditions are not specified since the analysis focus on steady-state. The mass flow rate of gas is kept constant. Ideal gas behavior is assumed for the gas mixture.

The molecular diffusion coefficients are calculated from the Chapmann-Enskog model for diluted mixtures (Bird et al., 1960) assuming binary diffusion of each species in a nitrogen gas. These values are then correlated in the form

$$D_{i,m} = \frac{a\left(T/300\right)^b}{p/101325}$$

where T is the gas temperature in K and p is the gas pressure in Pa. Table 2 shows the values for the constants a and b for the species considered. Table 2 also shows the heat of reaction associated to each species i.

The axial mass and thermal dispersions are estimated assuming laminar flow in a circular channel, i.e.,

$$\frac{D_{x,m}}{D_{i,m}} = \frac{Pe_m}{48}$$

$$\frac{D_{x,T}}{\alpha_g} = \frac{Pe_g}{48}$$

where the mass and thermal Peclet numbers are

$$Pe_m = \frac{u_g D_h}{D_{i,m}}$$

$$Pe_g = \frac{u_g D_h}{\alpha_g}$$

As an approximation, the channel diameter is modeled using a hydraulic diameter as

$$D_h = \frac{2bh}{(h+b)}$$

The interfacial surface-convection heat transfer coefficient is obtained from the solution of a laminar non-reactive flow in a square channel (Bird et al., 1960). From the Nusselt number, the interfacial heat transfer coefficient is obtained from

$$Nu = \frac{h_{sg} D_h}{\lambda_g}$$

The external surface-convection heat transfer coefficient is representative of a cylinder in a turbulent cross flow and is kept constant. Gas and solid thermal conductivities and heat capacities are estimated at an averaged temperature and kept constant. Table 3 shows the values used.

Table 2. Values for the molecular diffusion coefficients and enthalpy of reaction.

Specie	$D_{i,m}$	m^2/s	$\Delta h_{i,r}$
	a, m^2/s	b	J/kg
CH_4	0.216×10^{-4}	1.750	-4.67×10^6
H_2O	0.303×10^{-4}	1.632	-13.43×10^6
H_2	0.787×10^{-4}	1.750	00
CO	0.216×10^{-4}	1.730	-3.95×10^6
CO_2	0.177×10^{-4}	1.755	-8.94×10^6

Table 3. Values and parameters for the transport, heat transfer and mass transfer coefficients.

Parameter			Value
Gas specific heat	$c_{p,g}$	J/kg-K	1546
Gas thermal conductivity	λ_g	W/m-K	0.03
Solid density	ρ_s	kg/m^3	0.3160
Solid specific heat	$c_{p,s}$	J/kg-K	0.675
Solid thermal conductivity	λ_s	W/m-K	5.0
Channel Nusselt number	Nu		2.976
Channel Sherwood number	Sh		2.976
External heat transfer coefficient	h_e	W/m^2-K	100

3.2 MICROSCOPIC MODEL

The microscopic model considers the diffusion and chemical reaction in the washcoat and, considering the difference in length scales; it is treated as a one-dimensional problem. The volume-averaged species i conservation equation, assuming a purely diffusive process (in a diluted mixture approximation), written in molar units is

$$0 = \frac{d}{dz}\left(\varepsilon_\gamma c_g D_{i,e} \frac{dX_i}{dz} \right) + \varepsilon_\gamma \frac{\dot{w}_{r,i,\sigma}}{M_i} \qquad 6$$

where ε_γ is the porosity of the washcoat (phase σ), $D_{i,e}$ is the isotropic washcoat effective mass diffusivity of species i, and M_i is the molecular weight of species i. Considering that the gas species are diluted with nitrogen, a more rigorous Stefan-Maxwell formulation is not necessary and a simple binary diffusion modeled by Fick's law is accurate enough.

The volumetric σ-phase mass chemical reaction rate is related to the intrinsic molar surface reaction rate by

$$\dot{w}_{r,i,\sigma} = \dot{r}_{r,i,\sigma} \rho_{cat} M_i \qquad 7$$

where ρ_{cat} is the volumetric concentration of catalyst particles (per volume of σ-phase).

For a constant pressure and temperature mixture, Eq. (7) can be rewritten in terms of the molar fraction, becoming,

$$0 = \frac{d^2 X_i}{dz^2} + \frac{\rho_{cat}}{c_{g,\sigma} D_{i,e}} \dot{r}_{r,i,\sigma} \qquad 8$$

The boundary conditions for the microscopic model are:

$$\text{At } z = 0, \ \frac{dX_i}{dz} = 0.$$
$$\text{At } z = L_w, \ X_i = X_{\beta\sigma,i} \qquad 9$$

The interfacial mole fraction of the chemical species i $X_{\beta\sigma,i}$ is not known a priori, but is a result of the coupling between the microscopic and the macroscopic models as shown in the following.

The washcoat effective diffusivity is calculated from a model developed by Merzedur and Kaviany (2001),

$$\frac{D_{i,e}}{D_{i,m}} = \left(1 - \left(1 - \varepsilon_\gamma \right) \right)^{0.46}$$

3.3 COUPLING THE MICRO AND MACRO MODELS

The micro and macro models are coupled through the mass fluxes at the β-σ interface. The microscopic model is solved using an interface molar fraction $X_{\beta\sigma,i}$ as boundary condition. This condition is initially guessed. From the solution of the microscopic model, the species mass fluxes at the β-σ interface can be expressed as:

$$\dot{m}_{\beta\sigma,i} = \left[-c_g D_{i,e} \frac{dX_i}{dz}\bigg|_{z=L\sigma} \right] M_i \qquad 10$$

The volumetric reaction rate in the macroscopic model is obtained from the mass flux coming from the microscopic model in the $\beta\sigma$ interface by

$$\dot{w}_{r,i,\beta} = \dot{m}_{\beta\sigma,i} \frac{S_{\beta\sigma}}{\varepsilon_\beta} \qquad 11$$

where ε_β is the porosity, and $S_{\beta\sigma}$, is the specific interfacial area of the β phase. Then, the macroscopic model is solved and returns the volume-averaged value for the species concentration at the β (channel bulk) phase $c_{\beta,i} = Y_i \cdot \rho_g / M_i$. A surface mass convection model then requires that

$$\dot{m}_{\beta\sigma,i} = \frac{Sh_{\beta\sigma,i}D_{i,m}}{D_\beta}\left(c_{\beta\sigma,i} - c_{\beta,i}\right) \qquad 12$$

and this provides a new estimate for the washcoat species surface concentration $X_{\beta\sigma,i} = c_{\beta\sigma,i} / c_{\beta\sigma}$. Then, by an iterative process between the macroscopic and microscopic formulations, a final converged solution is obtained.

The microscopic model is solved as a sub-grid model for each numeric cell in the macroscopic model. From this solution, the value of the volume-averaged reaction rate becomes available and allows for the solution of the macroscopic model. After obtaining the β phase (bulk) species concentration, the interface mass concentration is calculated. This new value of surface concentration allows for new iteration in the microscopic model. In order to reduce the computational time, each solution of the microscopic model starts from the solution for the preceding node. This was responsible for a considerable reduction in computational time. The final solution is obtained when the variation in the parameters calculated drop bellow a convergence criteria. The solution of the equations requires a chemical kinetic model for the surface reactions, and this is reviewed next.

3.4 SURFACE CHEMICAL REACTION RATE MODEL

The solution of the microscopic model requires a chemical kinetic mechanism and expressions for the elementary reaction rates. Most results available in the literature for alumina supported nickel catalysts point to a Langmuir-Hinshelwood kinetic mechanism. Xu and Froment (1989) developed a 13-step mechanism from which 3 reactions are selected assuming that the surface reaction is the rate determining step. These three reactions divide the same active sites and for this reason the reaction rates share the same denominator which acts as an inhibitor. The elementary reaction rates can be written as

$$r_1 = \frac{\dfrac{k_{c1}}{p_{H_2}^{2.5}}\left(p_{CH_4}p_{H_2O} - \dfrac{p_{H_2}^3 p_{CO}}{K_{e1}}\right)}{\left(DEN\right)^2} \qquad 13$$

$$r_2 = \frac{\dfrac{k_{c2}}{p_{H_2}}\left(p_{CO}p_{H_2O} - \dfrac{p_{H_2}p_{CO_2}}{K_{e2}}\right)}{\left(DEN\right)^2} \qquad 14$$

$$r_3 = \frac{\dfrac{k_{c3}}{p_{H_2}^{3.5}}\left(p_{CH_4}p_{H_2O}^2 - \dfrac{p_{H_2}^4 p_{CO_2}}{K_{e3}}\right)}{\left(DEN\right)^2} \qquad 15$$

The inhibition term is:

$$DEN = 1 + K_{aCO}p_{CO} + K_{aH_2}p_{H_2} + K_{aCH_4}p_{CH_4} + \frac{K_{aH_2O}p_{H_2O}}{p_{H_2}} \qquad 16$$

In these equations, p_i is the species-i partial pressure (Pa), k_{ci} is the kinetic constant, K_{ei} is the chemical equilibrium constant and K_{ai} is the adsorption equilibrium constant. Using the set of parameters shown below, the reaction rates r_i return in kmol/kg$_{cat}$-s. The values of the activation energy satisfy Arrhenius equations and the enthalpies satisfy Van´t Hoff equations. Then, for the kinetic constant we have:

$$k_{ci} = A(k_{ci})\exp\left(-\frac{E_i}{RT}\right) \qquad 17$$

where

$$A(k_{ci}) = k_{ci,T_r}\exp\left(\frac{E_i}{RT_r}\right) \qquad 18$$

Here, $A\left(k_{ci}\right)$ is the pre exponential coefficient for the kinetic constant, E_i is the activation energy, R is the universal gas constant (8314.172 J/kmol-K) and T_r the temperature of reference.

For the adsorption constant we have;

$$K_{a\,j} = A\left(K_{a\,j}\right)\exp\left(-\frac{\Delta H_j}{RT}\right)$$

19

where

$$A(K_{a\,j}) = K_{a\,j,T_r}\,\exp\left[\frac{\Delta H_j}{RT_r}\right]\ j=1,2,3,4$$

20

Here, $A\left(K_{a\,j}\right)$ is the pre exponential coefficient for the adsorption constant, and ΔH_j is the adsorption enthalpy change.

From the chemical kinetic mechanism, the formation and destruction rates of the chemical species are calculated from

$$
\begin{aligned}
r_{CH_4} &= -\left(r_1 + r_3\right)\\
r_{H_2O} &= -r_1 - r_2 - 2r_3\\
r_{H_2} &= 3r_1 + r_2 + 4r_3\\
r_{CO} &= r_1 - r_2\\
r_{CO_2} &= r_2 + r_3
\end{aligned}
$$

21

In order to select appropriate kinetic parameters, 10 sets of kinetic parameters available in the literature were converted for the same basis kmol/kg$_{cat}$-s and compared under the same set of temperature and pressures (Garcia and Oliveira, 2006). Large discrepancies were found among the reaction rates predicted from these parameters. A few differences were found to be related to typographic errors when the parameters were listed on the references. Other differences, however, seem to be related to differences in behavior between the different catalyst particles and supports tested by the different authors. In order to be able to generate data that could be compared to most of the literature available, the well known parameters provided by Xu and Froment (1989) were selected, since these have been the most widely used for steam-reforming design. The parameters of the equations for the kinetic and adsorption constants are summarized in Table 4. The kinetic and adsorption parameters have units such that the intrinsic reaction rates result in kmol/kg$_{cat}$-s.

Table 4 Parameters for the kinetic and adsorption constants used in the simulation.

Parameters for the chemical kinetic constants			Parameters for the adsorption constants			
Reaction 1	Reaction 2	Reaction 3	CH_4	H_2O	H_2	CO
$E_{(1)}$ [kJ/mol]	$E_{(2)}$ [kJ/mol]	$E_{(3)}$ [kJ/mol]	$DH_{(CH4)}$ [kJ/mol]	$DH_{(H2O)}$ [kJ/mol]	$DH_{(H2)}$ [kJ/mol]	$DH_{(CO)}$ [kJ/mol]
240.1	67.13	243.9	-38.28	88.68	-82.9	-70.65
$k_{cT\,(1)}$	$k_{cT\,(2)}$	$k_{cT\,(3)}$	$K_{aT(CH4)}$	$K_{aT(H2O)}$	$K_{aT(H2)}$	$K_{aT(CO)}$
1.842×10^{-4}	7.558	2.193×10^{-5}	0.1791	0.4152	0.0296	40.91

Next, the results of the model are presented.

4. RESULTS AND ANALYSIS

From the thermal and equilibrium analysis, five basic conditions of temperature and steam to methane ratio were selected for the calculations, as presented in Table 5.

Table 5 Temperature and molar ratio conditions selected for the simulation

T° C	Methane to steam molar ration		
	3:1	4:1	5:1
650	x		x
700		x	
750	x		x

The pressure was kept at 1.2 bar. The external ambient temperature was set to the inlet gas temperature. Other properties and conditions are listed in Table 6.

Table 6 Conditions selected for the simulations.

Parameter			Value
Total pressure	p	bar	1.2
Gas mass flow rate	m_g	kg/s	15×10^{-3}
Monolith length	L_β	m	0.15
Monolith diameter	D_m	m	0.03
Channel cross section	$h = b$	m	0.0015
Washcoat thickness	L_σ	m	50×10^{-6}
Number of channels per inch squared	ppis		400
Porosity of the monolith	ε_β	$m^3{}_{pore}/m^3{}_{MONOLITH}$	0.595
Porosity of the washcoat	ε_γ	$m^3{}_{pore}/m^3{}_{WASHCOAT}$	0.72
Catalyst mass per volume of porous medium	ρ_{cat}	$kg_{cat}/m^3{}_{WASHCOAT}$	44.0
Washcoat effective diffusivity	$D_{i,e}$	m^2/s	5.0

Here, the interest lies in compact, small size reactors. Then, the simulations are restricted to a small diameter reactor. Analysis of the radial heat transfer conduction resistance shows that a radially lumped model is a good approximation for monolith diameters smaller than 3 cm (Garcia, 2006).

In all figures presented, the ordinate axis represents the monolith axial coordinate divided by the monolith length. The legends indicate the absolute inlet gas temperature and the steam-to-methane molar ratio (T(K) - R). Figure 4(a) presents the variation of the gas temperature along the reactor length for the five temperature/steam-methane ratios simulated. It can be observed that the gas flow enters the reactor at the inlet temperature specified and its temperature decreases along the reactor due to the endothermic behavior of the global reaction. Figure 4(b) presents the axial variation of the solid temperature. At the reactor inlet, the strong reaction rates cause a sharp decrease of the solid temperature. As the reaction rate drops along the reactor, the solid temperature reaches a plateau with temperature close to the external ambient temperature even, as a result of the heat transfer to the external environment.
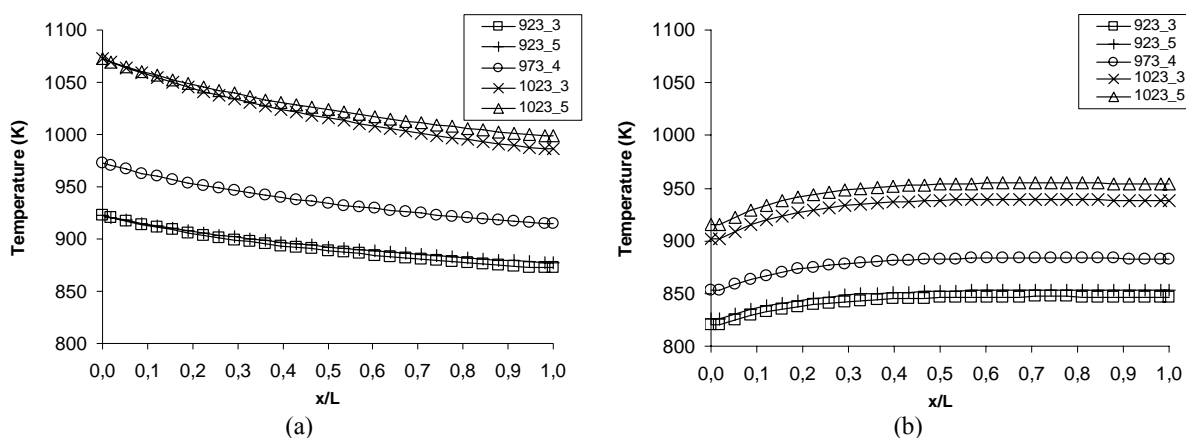

Figure 4. (a) Axial gas temperature variation and (b) axial solid temperature variation along the reactor for the five conditions simulated. The legends indicate the absolute inlet gas temperature and the steam-to-methane molar ratio (T(K) _ R).

Figure 5 presents the β-σ interface mass reaction rate for methane. The reaction rate reaches its peak value in the first 5% of the reactor length and after approximately 30% of the reactor length, the reaction rate drops to much smaller values. The same trend is observed for all the inlet conditions examined. This reveals that the reactor activity drops sharply once the methane concentration is reduced.
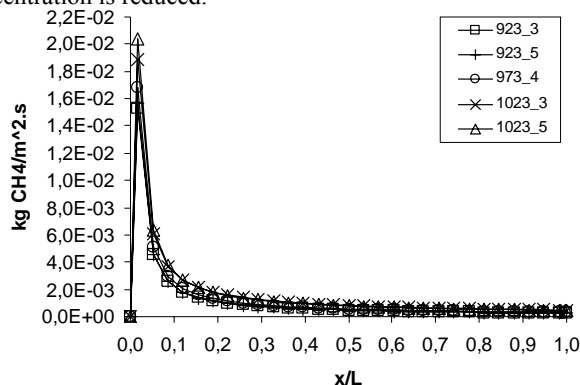

Figure 5. Surface mass reaction rate for methane at the β-σ interface.

Figure 6 presents the axial mole fraction of (a) H_2 and (b) CO along the reactor. Both H_2 and CO mole fractions increase as reaction proceeds along the reactor. From the inlet conditions examined, the higher hydrogen production is achieved for 750°C (1023 K) / R = 3:1 and the minimum is achieved at 650°C (923 K) / R = 5:1 showing the more important role of reaction temperature when compared to the steam-to-methane molar ratio. Increasing the steam-methane ratio for the same temperature reduces the mole fraction of H_2, due to the excess water present as product. The approach to equilibrium can be observed when we compare the values reported in Table 1 to the values obtained in this calculation. Table 1 reports an equilibrium mole concentration of H_2 at 700°C (973 K) and R = 4 of 0.7764 dry base, equivalent to 0.4985 wet base. The value obtained from Figure 6 at the end of the reactor for the same conditions is 0.045091, representing a difference of 90.95% of the equilibrium data. Therefore, the gas stream is still far from equilibrium. Even at the higher temperature (1023 K) and R = 5, the difference between the equilibrium value and the value at the end of the reactor is 86.77 % of the equilibrium data.

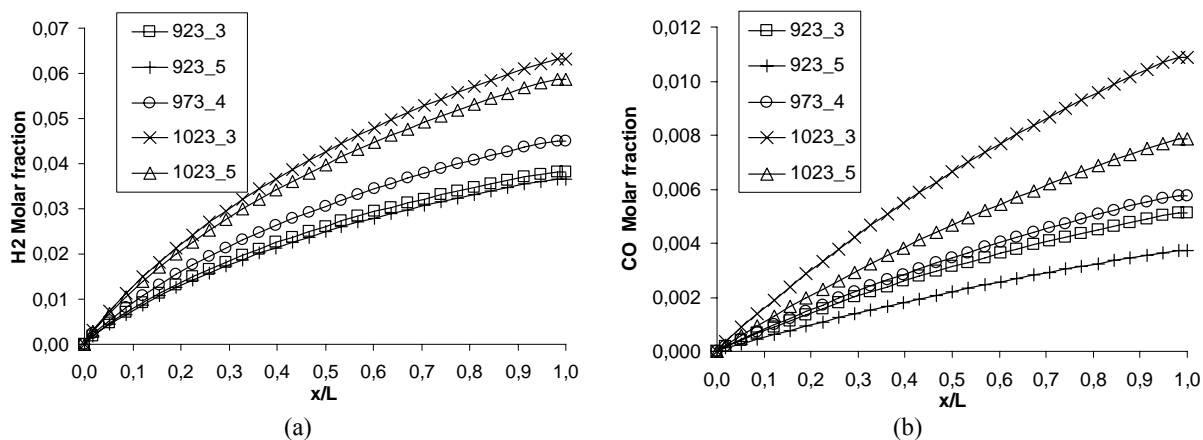The CO production, shown in Figure 6(b), is high, achieving values above 3000 ppm at the exit.

(a)

(b)

Figure 6. Axial variation of (a) H_2 and (b) CO mole fraction along the reactor.

The existence of diffusion limitations can be assessed calculating the local washcoat internal effectiveness factor and the local Thiele modulus (the Damköhler number) along the reactor. The washcoat effectiveness is defined as the ratio between the local actual reaction rate and the reaction rate that would exist under no diffusion resistance across the washcoat. It is calculated from

$$\eta = \frac{\dot{m}_{\beta\sigma,i}}{\left(\dot{m}_{\beta\sigma,i}\right)_{max}}$$

22

where $\dot{m}_{k,\beta\sigma}$, is the mass flux of the k component in the $\beta\sigma$ interface. The smaller the value of the internal washcoat effectiveness, the higher is the role of diffusion as a controlling mechanism.

The Thiele modulus (an "observed" Thiele modulus) is defined as:

$$\phi_i^2 = \frac{\dot{m}_{\beta\sigma,i}L_\sigma}{M_i c_{g,\beta\sigma} X_{\beta\sigma,i} D_{i,e}}$$

23

where L_σ is the washcoat thickness, M_k is the molecular mass of the k component, $c_{g,\beta\sigma}$ is the molar concentration in the $\beta\sigma$ interface, $X_{k,\beta\sigma}$ is the mole fraction of the k component in the $\beta\sigma$ interface and $D_{i,e}$ it the effective diffusivity of species i in the washcoat. All variables are evaluated locally, i.e., at a given location along the reactor length.

The Thiele modulus indicate the ratio between the diffusion characteristic time scale and the chemical kinetic characteristic time scale. A high value for the Thiele modulus implies that chemical kinetics is faster than diffusion.

Figure 7 presents the local internal effectiveness factor (a) along the reactor and (b) as a function of the Thiele modulus calculated for methane. In Figure 7(a) it is observed that the effectiveness factor is small at the channel entrance because of the high reaction rates. As a result, there is a poor use of the catalyst sites buried deep in the washcoat, since most of the reaction occurs at a region close to the $\beta\sigma$ interface. As the reaction rate decreases along the reactor, the effectiveness factor increases reaching 0.99 at the reactor outlet. There, diffusion is no longer limiting the reaction rates observed. Since diffusion is limiting along most of the reactor, the temperature and the steam-methane ratio has a small effect on the local internal effectiveness factor. Figure 7(b) shows the local internal effectiveness factor plotted against the local Thiele modulus. The Thiele modulus is higher at the reactor inlet, where methane concentration and temperature are higher resulting in larger reaction rate. We note that for all the conditions tested the methane conversion is mostly diffusion limited. For a given effectiveness, higher temperatures result in higher local Thiele modulus, indicating a faster kinetic when compared to diffusion. The curves do not collapse to a single one due to the complexity of the chemical reaction mechanism (Fogler, 2005).
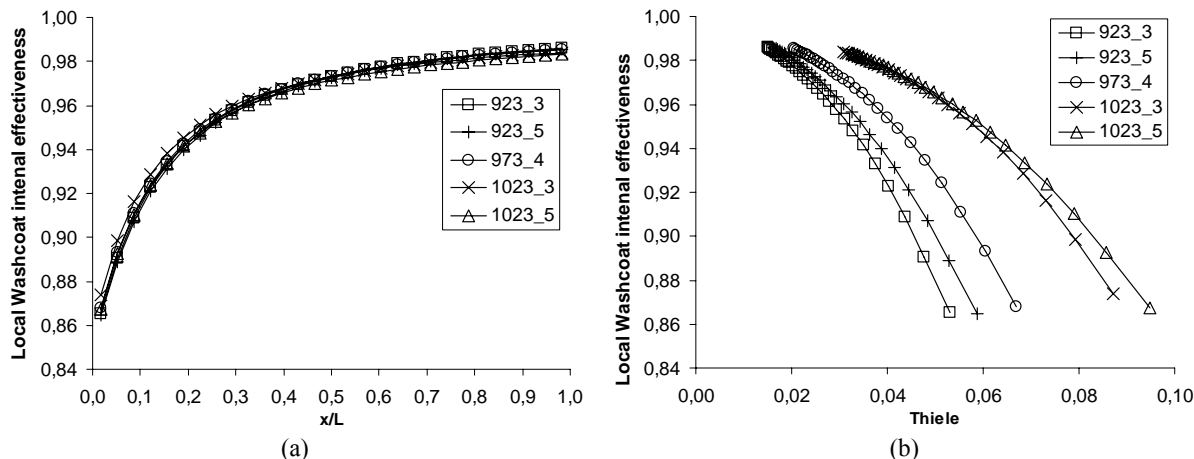

Figure 7 Local washcoat internal effectiveness as a function of (a) reactor length and (b) local Thiele modulus (Damköhler number).

Figure 8 presents the total conversion (at the reactor outlet) for the CH_4 and H_2O, the total yield of H_2, CO and CO_2, and the selectivity of the H_2 in respect to CO. These are calculated according to the classical definitions as follows:

$$\eta_{L,CH_4} = \frac{c_{g,0}X_{CH4,0} - c_{g,L}X_{CH4,L}}{c_{g,0}X_{CH4,0}}$$

24

$$y_{L,k}^1 = \frac{c_{g,L}X_{i,L} - c_{g,0}X_{i,0}}{c_{g,0}X_{CH4,0}}$$

25

$$S_{L,H2} = \frac{c_{g,L}X_{H2,L} - c_{g,0}X_{H2,0}}{c_{g,L}X_{CO,L} - c_{g,0}X_{CO,0}}$$

26

It is observed that the temperature has a stronger effect than steam-methane ratio. The CH_4 conversion is higher at the higher temperatures, remaining approximately constant when R is increased from 3 to 5. H_2O conversion drops when R is changed from 3 to 5 because of the excess water remaining. The H_2 yield also increases with temperature and is less sensitive to R. The CO production at 650^oC is smaller at the steam-methane ratio R = 5 than at R = 3. This effect is a result of the displacement of the equilibrium of the water-gas shift reaction to the production of CO_2. The CO2 yield increases with R for the same reason. The selectivity of H_2 to CO increases with the steam-methane molar ratio and decreases with an increase in temperature. Both behaviors result primarily from the equilibrium of the water-gas shift reaction. The selectivity of H_2 to CO reaches a maximum, for the conditions tested, at 650^oC / R = 5, reaching 10 moles of H_2 for 1 mole of CO. However, this is not of a great advantage, since the outlet molar fraction of CO, under these conditions is still high, requiring further CO removal operations.
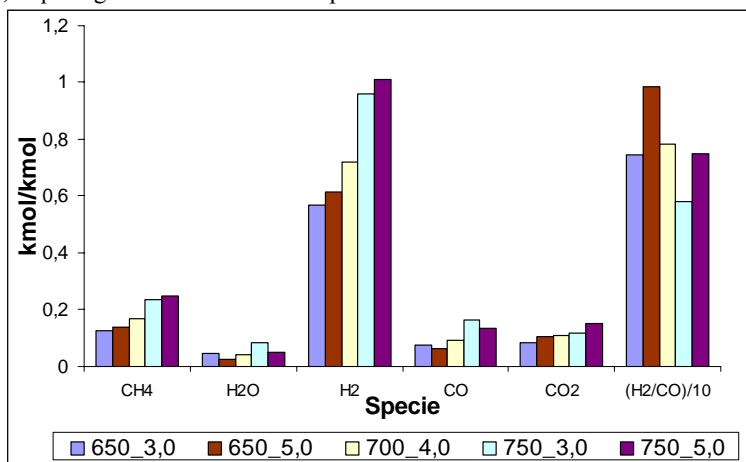

Figure 8 Total conversion (CH_4 and H_2O), total production (H_2, CO and CO_2) and selectivity (H_2/CO)/10 for the conditions tested [T(^oC) – R].

5. CONCLUSION

A thermodynamic equilibrium analysis allows the calculation of the limiting equilibrium conditions for the products mole fractions and also the equilibrium heat transfer rates required, but does give indications of the proper size for a reforming reactor. With this objective, a two-level heat and mass transfer model was developed to allow for the study of the diffusion limitations imposed by the monolith reactor and to check the possibility of reaching equilibrium conditions in a short, compact reactor. The mass flow rate of methane was selected such as to produce 5 kW of electrical power in a PEM fuel cell operating at 80^oC with 0.5 electrical efficiency. The reforming temperature and steam-to-methane molar ratio were varied around a base value in order to estimate the sensitivity of the reactor performance with respect to reforming conditions. The catalyst load was assumed uniform across the washcoat and along the reactor.

 The results show that:
1. The entrance of the reactor is chemically more active. A high reaction rate peak is observed in the first 5% of the reactor length. In this position, the heat transfer rate from the external ambient to the gas phase (across de solid phase) is not high enough to guarantee that the reactor remain isothermal at the inlet condition. In a 15 cm reactor the gas phase temperature drops as much as 60^oC from the inlet temperature. In this region, the internal washcoat effectiveness is around 0.87 showing that the reaction conditions are diffusion controlled.
2. Comparing the reactor outlet H_2 mole fraction to the equilibrium mole fraction it is shown that the reactor is far from achieving equilibrium conditions. . For reactor temperature of 700^oC and steam-to-methane molar ratio of 4 the difference between the outlet mole fraction and the equilibrium mole fraction is 90.95% of the equilibrium data.
3. For a constant pressure of 1.2 bar, high hydrogen production is obtained at 750^oC and steam-to-methane molar ratio between 3 and 4, but the higher selectivity in respect to CO is obtained at steam to methane molar ratio of 5 in temperatures between 650^oC and 750^oC. However, even at the higher selectivity, an amount of CO between 7000 and 11000 ppm exists at the reactor outlet.

 As a general conclusion, we can observe that the use of a monolith reactor for steam reforming is possible, but still better heat and mass transfer needs to be achieved at the reactor inlet in order to obtain a more compact reactor. One possibility to increase conversion would be to distribute the reactants mass flow rate in a larger number of monoliths in order to increase the mixture residence time within the reactor without reducing each monolith's heat transfer resistance to the external environment. Finally, the advantage of the use of flow reversal in obtaining higher conversion should be

tested. A transient implementation of the model, with a proper account for the adsorption transient kinetics, should allow the computations for oscillating flow.

Aknowledgements:

6. REFERENCES

BIRD, R. B., STERWART, W. E., LIGHTFOOT, E. N., 1960, Transport Phenomena, John Wiley, New York.

BIYIKOGLU, A., 2005, Review of proton exchange membrane fuel cell models, International Journal or Hydrogen Energy, vol. 30, pp. 1181–1212.

DOKUPIL, M., SPITTA, C., MATHIAK, J., BECKHAUS, P. AND HEINZEL, A., 2006, Compact propane fuel processor for auxiliary power unit application, Journal of Power Sources, Vol. 157, pp. 906-913.

FOGLER, H. Scott. Elements of chemical reaction engineering. 3. ed. New York: Prentice Hall, 1999. 967 p.

GARCIA, L. E. A., 2006, Development of a monolithic steam reforming reactor for hydrogen production for fuel cells, Master Thesis (in Portuguese), Programa de Pós-Graduação em Engenharia Mecânica, UFSC.

GARCIA, L. E. A. and OLIVEIRA, A. A. M., 2006, Thermodynamic and chemical kinetic analysis of a 5 kw, compact steam reformer – PEMFC system, Proceedings of ENCIT 2006, ABCM, Curitiba, Brazil, Dec. 5-8.

KAVIANY, M., 1995, Principles of Heat Transfer in Porous Media, 2nd. Edition, Springer, New York.

MATHIAK, J., HEINZEL, A., ROES, J., KALK, Th., KRAUS, H. and BRANDT, H., 2004, Coupling of a 2.5 kW steam reformer with a 1 kWel PEM fuel cell, Journal of Power Sources, v. 131, pp. 112-119.

TWIGG, V. M., 1989, Catalyst Handbook, 2nd edition, Wolfe Publishing Ltd, Cleveland.

XIU, G., SOARES, J. L. and RODRIGUES, A. E., 2002, Simulation of five-step one-bed sorption-enhanced reaction process, AIChE Journal. v. 48, n.12, p. 2817-2832.

XIU, G., LI, P. and RODRIGUES, A. E., 2003, Adsorption-enhanced steam-methane reforming with intraparticle-diffusion limitations, Chemical Engineering Journal, v. 95, pp. 83-93.

XU, J. and FROMENT, G. F., 1989, Methane steam reforming, methanation and water-gas shift: I. Intrinsic kinetics, AIChE Journal, v. 35, n.1, pp. 88-96.